Flashback prevention in a hydrogen-fueled reheat combustor by water injection optimized with global sensitivity analysis

Pousada, Pablo Rouco; Doan, Nguyen Anh Khoa; Aditya, Konduri; Düsing, Michael; Ciani, Andrea; Langella, Ivan

GT2024-127332

FLASHBACK PREVENTION IN A HYDROGEN-FUELED REHEAT COMBUSTOR BY WATER INJECTION OPTIMIZED WITH GLOBAL SENSITIVITY ANALYSIS

Pablo Rouco Pousada[1,*], Nguyen Anh Khoa Doan [1], Konduri Aditya [2], Michael Düsing[3], Andrea Ciani [3], Ivan Langella[1]

[1]Faculty of Aerospace Engineering, Technical University of Delft, Delft, Netherlands
[2]Department of Computational and Data Sciences, Indian Institute of Science, Bengaluru, India
[3]Ansaldo Energia Switzerland AG, Baden, Switzerland

ABSTRACT

This paper investigates water injection effects in a simplified Ansaldo GT36 reheat system under realistic conditions of 20 atm using large eddy simulation (LES) coupled with thickened flame modeling and adaptive mesh refinement. The water injection conditions are optimized by performing a parametric study based on global sensitivity analysis with a surrogate model based on Gaussian process to reduce computational cost. In particular, the influence of four design parameters, namely Sauter mean diameter, water mass flow and the angles of the spray's hollow cone, is tested to achieve an optimized solution. In the 'dry' case, the LES simulations show several flashback events attributed to compressive pressure waves resulting from autoignition in the core flow near the crossover temperature. The use of water injection is found to be effective in suppressing the flashback occurrence. In particular, the global sensitivity analysis shows that the external angle of the spray cone and the mass flow of water are the most important design parameters for flashback prevention. NOx emissions are reduced by about 17% with water injection. Once an optimized condition with water injection is found, a recently proposed method to downscale the combustor to lower pressures is applied and tested. Additional LES are performed for this purpose at the 'dry', unstable condition and the 'wet', stable condition. Results show that similar dynamics are predicted at 1 atm, validating the method's robustness. This provides avenues for experimentally testing combustion dynamics at simplified conditions which are still representative of high-pressure practical configurations.

Keywords: Fuels and combustion, Gas turbines, Design optimization, Emissions, Sprays

1. INTRODUCTION

The recent focus on environment and sustainability has led to a significant ongoing shift in the power generation sector from conventional fossil fuels to more sustainable alternatives. Among these, hydrogen stands out as a promising solution for clean energy generation [1]. Nevertheless, hydrogen flames pose major challenges, such as formation of relatively high levels nitric oxides (NOx), which have a high global warming potential [2]. Moreover, hydrogen is characterized by its wide flammability range, very high flame propagation speed, and high diffusivity and reactivity [3]. As compared to natural gas, these properties pose more stringent requirements on the combustor design [4].

One way to reduce NOx and simultaneously prevent possible flashback events, is to inject a certain amount of water within the combustion chamber. This is particularly relevant in the case of reheat systems, where the injection of water in liquid or steam form, by reducing the temperature near the flame region, increases the autoignition delay time, allowing for an effective control of the flame position in the combustor. The temperature decrease near the flame also implies that NOx is reduced mainly due to the Zeldovich pathway, but also by the reduction of O radicals [5]. Several studies have investigated the injection of water in gas turbine combustors since the 1970s [6], but interest in this technology for practical devices grew dim partly due to the widespread use of dry low NOx premixed combustion [7], and partly because water injection can cause local extinctions, which in turn increase CO levels and inefficiency [8]. With the increased emphasis on hydrogen combustion by manufacturers, water injection has been re-considered in recent years as a useful technology to reduce NOx levels. Being carbon-free, no CO can in fact be emitted in the hydrogen flame, and hydrogen's strong reactivity further implies that local extinctions are unlikely.

The performance of water injection depends on several parameters including, but not limited to, injection angle and position, water to fuel ratio, diameter, temperature, and state (steam or liquid). Amani *et al*. [9] achieved 87% reduction in NOx by optimizing several parameters of the combustor and water injection. A swirl number of 1.96, a small injection angle, and

*Corresponding author: p.roucopousada@tudelft.nl
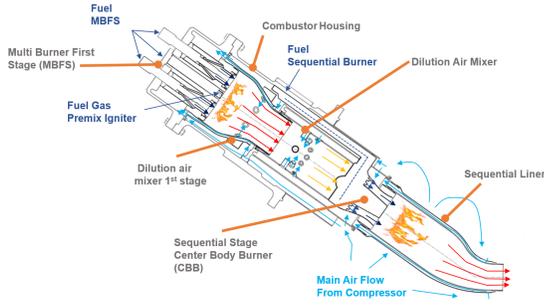
FIGURE 1: Schematic of the combustor within the Ansaldo GT36. [19]

a water-to-fuel massflow ratio between 2 and 3.4 were found to be the optimal parameters. Farokhipour *et al.* [10] found, for a swirl-stabilized configuration, that the injection angle and injector position must ensure that droplets do not end trapped within the internal recirculating zone (IRZ), and found an optimized water-to-fuel massflow ratio of about 1. Pappa *et al.* [11] demonstrated that water injection can prevent flashback in micro gas turbines fuelled by hydrogen-enriched methane. Most previous studies, however, explored combustion at atmospheric conditions, which do not represent the conditions under which a gas turbine operates, and therefore conclusions drawn are of limited relevance [12]. Moreover, use of pure hydrogen in practical devices is a challenge due to its strong reactivity and diffusivity, and only relatively recently technologies are being proposed where hydrogen can be burnt safely in high concentrations [13]. One such technology is the constant pressure sequential combustion (CPSC) used in the Ansaldo Energia GT36, which consists of two combustor stages operating in lean premixed conditions. In the first stage, the flame is stabilized by flame propagation, which allows for good stability and relatively mild exhaust temperatures required as inlet in the second stage. The second stage is mainly stabilized by means of autoignition, implying combustion can be controlled by the inlet temperature. For a reheat combustor, operative pressures of around 20 atm or above are commonly used [14], and only a limited number of studies have addressed these conditions [15, 16]. At such pressure compression heating produced by pressure waves travelling upstream was shown to reduce locally the autoignition delay time, [12, 17, 18], increasing the risk of flashback. This coupling between combustion dynamics and pressure waves can cause significant changes in the flame anchoring position along the centerline [18], which can lead to flashback. It is thus crucial to understand the combustion dynamics behind the operation of this type of burner at real pressure conditions in order to safely and efficiently operate it with hydrogen.

In the present study, large eddy simulations (LES) of a simplified geometry of the second stage of the state-of-the-art Ansaldo GT36 sequential combustor are used to investigate the flame dynamics under reheat conditions at 20 atm. A sketch of this combustor is provided in Fig. 1. The flame within this system was shown to stabilize by both means of flame propagation and autoignition, the latter being the dominant mechanism [14]. The LES are run using a thickened flame model [20] and an adaptive mesh refinement approach. At-off design conditions without

water injection, chosen here as baseline calculation, the LES predicts at 20 atm a highly unstable flame with wave-driven periodic flashback. Liquid water injection is then used to suppress the flashback, and an optimal performance in terms of NOx emission and flame stability (i.e. no flashback or strong oscillations observed) is found by the use of global sensitivity analysis, where a surrogate Gaussian model is used in order to reduce the amount of simulations to be performed to about 20. Further LES are then performed at 1 atm in the attempt to mimic the combustion dynamics at 20 atm. In fact, relatively recently, Rieth *et al.* [16] proposed a method to mimic the reactive flow conditions observed at high pressure by running less expensive simulations at atmospheric pressure. They show using DNS that this is possible by adjusting the equivalence ratio and reactant temperature and maintaining a set of non-dimensional parameters. This method is tested here for both (wet) stable and (dry) unstable conditions found for the high pressure case. The method is shown to work well for the unstable condition in the dry case (no water injection used), i.e. a similar flashback dynamics observed for the 20 atm case is found at 1 atm when using the operative conditions imposed by the method in [16]. Vice-versa, a stable condition is found at 20 atm without using water injection by starting from the stable condition at 1 atm found in a previous work [17]. The method is applied then to the wet case and an investigation is conducted to shed light on how the water injection parameters have to be scaled to maintain the same flame dynamic at low pressure.

The objectives of the present study are: i) to shed light on the flashback dynamics on the reheat combustor calculation at high pressure; ii) to use global sensitivity analysis to obtain a quantitative assessment of the conditions at which water has to be sprayed to suppress flashback and NOx without compromising on efficiency; and iii) to use the method proposed in [16] to downscale the combustor to lower pressures and extend it to also mimic water spray conditions. The remainder of this paper is organized as follows. In Section 2 combustion and spray models used in the LES are presented, along with details of the numerical solver. In Section 3 the global sensitivity analysis approach and surrogate model are introduced, along with the downscaling method. Results are presented in Section 4. Main conclusions and suggestions for future work are provided in Section 5.

2. NUMERICAL MODEL
2.1 Combustion, turbulence and chemical kinetics

The artificially thickened flame model formulation of Wang *et al.* [20] with dynamic local thickening is used to account for the wrinkling effect of turbulence on the flame at the subgrid scale. The flame is thickened based on an efficiency factor E and a local thickening factor F, whose value is $F > 1$ near the flame front and $F = 1$ away from the flame. The conservation equation for species i within this approach reads:

$$\frac{\partial \rho Y_\alpha}{\partial t} + \frac{\partial \rho Y_\alpha u_j}{\partial x_j} = \frac{\partial}{\partial x_j}\left(\rho E F D_\alpha \frac{\partial Y_\alpha}{\partial x_j}\right) + \frac{E}{F}\dot{\omega}_\alpha \qquad (1)$$

where ρ is the mixture density, u_j is the velocity component in direction j and $\dot{\omega}_\alpha$ is the reaction rate of species α per unit of mass. Based on the maximum thickness factor $F_{max} = n_{res}\Delta_x/\delta_l$, F can be calculated locally as $F = 1 + (F_{max} - 1)S$, where n_{res} is

Copyright © 2024 by ASME

the number of numerical cells across the flame, δ_l is the laminar flame thickness and Δ_x the local grid spacing. The sensor S is determined as [21]:

$$S = \max\left[\min\left(\beta\frac{|\bar{\omega}_{\text{sens}}|}{\dot{\Omega}_{\text{sens},0}(\phi)} - 1, 1\right), 0\right] \tag{2}$$

with $|\bar{\omega}_{\text{sens}}|$ being the local reaction rate, β a modelling coefficient and $\dot{\Omega}_{\text{sens},0}$ the maximum reaction rate of the sensor from a 1D laminar flame at a given equivalence ratio.

The efficiency factor $E = \Xi|_{\delta=\delta_l}/\Xi|_{\delta=F\delta_l}$ is used to quantify the reduction in the subgrid flame surface area resulting from the thickening process, where the wrinkling factor for scale Δ is modelled according to Charlotte *et al.* [22]: as

$$\Xi_\Delta = \left(1 + \min\left[\frac{\Delta}{\delta_l} - 1, \Gamma_\Delta\left(\frac{\Delta}{\delta_l}, \frac{u'_\Delta}{s_l}, \text{Re}_\Delta\right)\frac{u'_\Delta}{s_l}\right]\right)^\beta \tag{3}$$

In the equation above s_l is the laminar flame speed and u'_Δ is the subgrid scale velocity, which in the present model is assumed to be unaffected by the flame front. Γ_Δ is a factor that takes into account the straining effect of all turbulence scales smaller than Δ and Re_Δ is the subgrid scale Reynolds number.

The chemical mechanism employed is that of Li *et al.* [23], consisting of 11 species and 19 reactions. This mechanism was selected based on the good compromise between accuracy and computational cost [24], and the fact that the same mechanism was used in previous works on the same configuration to be studied here [14, 16–18].

2.2 Spray Model

The injection of liquid water is modeled through an Eulerian-Lagrangian formulation. No breakup model is used as the particle size is directly imposed by assigning the Sauter mean diameter (SMD) and using a Rosin-Rammler distribution. Also, secondary breakup and coalescence of particles are considered negligible (high Weber number). The cumulative probability describing this distribution is:

$$p(r) = 1 - exp\left(\zeta^{C_{RR}}\right) \quad \text{for } 0 < \zeta < \zeta_{max} \tag{4}$$

where $\zeta = r/\bar{r}$ and r and $\bar{r}$ are respectively droplet radius and its mean value calculated based on the SMD $d_{32} = 2r_{32}$ as $\bar{r} = \Gamma(1 - C_{RR}^{-1})r_{32}$. The parameter C_{RR} measures the spread of the droplet radius. The maximum value of ζ, $\zeta_{max} = \ln(1000)^{\frac{1}{C_{RR}}}$ is used to limit the maximum radius. The droplet velocity in direction i, c_i, is described by:

$$\frac{dc_i}{dt} = \frac{3}{8}\frac{\rho}{\rho_l}C_D\frac{|U_i|}{r}U_i \tag{5}$$

where the relative droplet-gas velocity for the direction i is defined as $U_i = \bar{u}_i + u'_i - c_i$, with $\bar{u}_i$ and u'_i being the mean local velocity and its fluctuation respectively, and ρ_l is the density of the droplet. The drag coefficient C_D is modelled assuming spherical droplets and in function of the droplet Reynolds number Re_d as

$$C_D = \begin{cases} \frac{24}{Re_d}\left(1 + \frac{1}{6}\text{Re}_d^{2/3}\right) & \text{Re}_d < 1000 \\ 0.424 & \text{Re}_d > 1000 \end{cases} \tag{6}$$

As droplets evaporate, their radius r_0 decreases, which in this work is modeled using the Frossling correlation [25]:

$$\frac{dr_0}{dt} = -\frac{\alpha_{\text{spray}}\rho_g D}{2\rho_l r_0}B_d\text{Sh}_d \tag{7}$$

where α_{spray} is the scaling factor for the mass transfer coefficient, D is the diffusivity of the liquid water in air, Sh is the Sherwood number and B_d is the Spalding mass transfer number. The Sherwood number is expressed as

$$\text{Sh}_d = \left(2.0 + 0.6\text{Re}_d^{1/2}\text{Sc}^{1/3}\right)\frac{\ln(1 + B_d)}{B_d} \tag{8}$$

where Sc is the Schmidt number of the droplet. The droplet temperature is found by applying an energy balance:

$$\rho_d\frac{4}{3}\pi r^3 C_\ell\frac{dT_d}{dt} - \rho_d 4\pi r^2\frac{dr_0}{dt}L_V = 4\pi r^2 Q_d \tag{9}$$

where L_v is the latent heat of vaporization, C_l is the liquid specific heat and Q_d the heat conduction rate found using the Ranz-Marshall correlation assuming that only conduction is important:

$$Q_d = \frac{K_{gas}(T - T_d)}{2r}\text{Nu}_d \tag{10}$$

In the above K_{gas} is an interpolation constant and Nu_d is the Nusselt number determined employing a correlation analogous to the one used for the Sherwood number:

$$\text{Nu}_d = \left(2.0 + 0.6\,\text{Re}_d^{1/2}\,\text{Pr}_d^{1/3}\right)\frac{\ln(1 + B_d)}{B_d} \tag{11}$$

where Pr_d is the temperature-dependent droplet Prandtl number. The above correlation was found to be satisfying for diluted sprays with droplet diameter below about 74 μm [26], which is above the average diameter observed for the simulations in the present study. Also the effect of turbulence on the heat and mass transfer from the droplet [27] was not taken into account for simplicity, assuming that the Kolmogorov's scale is comparable or larger than the droplet size, at least as the droplets approach the flame region [28]. The effect of modified droplet-flame interaction (due to the flame thickening) was also neglected for simplicity given the purposes of the present work, where the objective is to assess the relative effect of injection parameters.

Finally, the drop-wall interaction is modelled according to the Weber number We_i of the droplet at impact. If $We < 80$, the droplet rebounds elastically; if $We > 80$, the impinging droplet leaves tangent to the surface like a liquid jet. Collisions between droplets are also taken into account using the method of Schmidt and Rutland [29].

2.3 Case study and computational parameters

The case study is a simplified representation of the reheat combustor featuring the Ansaldo GT36 gas turbine, also used for previous works [14, 17]. This configuration, sketched in Fig. 2, consists of a mixing duct of dimension $3L \times 1L \times 1.5L$, where $L = 1$ cm, followed by a sudden expansion geometry and the main combustion chamber of dimensions $3L \times 2L \times 1.5L$. Therefore, the geometry employed in this study serves as a broad

simplification of the actual GT36 reheat combustor, aiming to capture its main characteristics while also being representative of other potential reheat combustors. As a result, the applicability of this study extends beyond the specific Ansaldo reheat combustor solutions and is intended to be of interest to a wider range of potential designs.

The following off design conditions have been used: at the inlet of the mixing duct burnt gases from the hydrogen combustion in the first stage (water vapour and excess air) are issued and diluted with additional air and hydrogen, resulting in an inlet temperature of 1180 K and an equivalence ratio $\phi = 0.35$. The bulk velocity at the inlet is $u_\infty = 200$ m/s, with a turbulence intensity of 10%, which is representative of a gas turbine combustor [14, 17]. The digital filter method has been applied to superimpose turbulent fluctuation, where rms values and length scales are taken from [14]. The walls of the burner are cooled to reach a constant temperature at steady state of about $T_w = 750$ K, which is a common value used by several authors dealing with reheat combustors [14, 17, 30, 31]. Although the choice of a constant temperature is a strong simplification, it allows us to abstract from specific cooling configurations or systems. The Werner and Wengle [32] law-of-the-wall model is used for the calculation of the wall stress, while the Han and Reitz model [33] is the one selected for the heat transfer. The flame in the combustor is stabilized on the centerline by means of autoignition, with its base located at the exit of the mixing tube, where the flame is stabilized in an assisted-ignition mode due to the recirculation zones forming as result of the sudden-expansion geometry. This point of operation results from the balance between the autoignition and residence time. The process of autoignition expands locally the gases, inducing pressure waves travelling both downstream and upstream, and leading to compression heating. At 20 atm, which is the operative condition of interest in the present work, this compression results in an early autoignition event with pressure waves travelling upstream and causing unwanted reactions in the mixing tube. For the studied geometry, which does not allow the pressure waves to dissipate properly, depending on the particular conditions, these reactions either induce an oscillatory movement of the flame front, or a flashback.

The equations for the LES include continuity, momentum and absolute enthalpy (sum of sensible and formation specific enthalpies) in addition to the specific combustion equations described in the previous section. The compressible flow equations are solved using Converge v.3.1.9 CFD software, which uses the finite volume approach and pressure implicit with splitting of operators (PISO) algorithm for the pressure-velocity coupling. A second-order central scheme is used for all transported quantities. An implicit Euler scheme is used for time marching, which provides excellent stability at a reduced computational expense. The time step is set to have a maximum Courant–Friedrichs–Lewy number of 1 for the entire domain, which reduces to a maximum of about 0.4 in the region of the flame, where the mesh is more refined. The unclosed subgrid stresses in the momentum equation are modelled with a one-equation viscosity model [34, 35]. Due to the relatively high level of turbulence in the combustor, a gradient hypothesis is used to close all turbulent transport terms in the scalar transport equations, with a subgrid Schmidt number
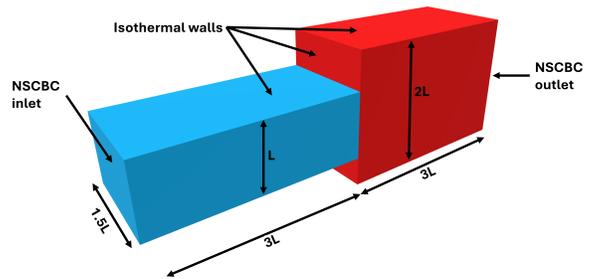
FIGURE 2: Computational domain and its boundaries.

(Prandtl number for enthalpy) set to 0.7. The laminar viscosity is computed via Sutherland's law. Density is computed from temperature and pressure using the Redlich-Kwong [36] state equation.

Boundary conditions are assigned as follows. A flat velocity profile is assigned at the inlet and turbulence is superimposed using the method in [34]. No-slip condition and constant temperature are assigned at the walls to mimic the wall cooling. Zero gradient condition is assigned at the walls and at the outlet for all other scalars. To deal with pressure waves bouncing within the combustor, the quasi non-reflective Navier Stokes characteristic boundary conditions (NSCBC) [37], with an under-relaxation factor of 0.25 and a characteristic length $L_{\text{NSCBC}} = 2L$, are assigned at inlet and outlet. The parameters for the NSCBC were found in a previous work [17] and guarantee that the operating pressure is maintained within the domain while allowing the pressure waves to partially exit the domain. The composition at the inlet consists of $Y_{\text{N}_2} = 0.749$, $Y_{\text{O}_2} = 0.178$, $Y_{\text{H}_2\text{O}} = 0.0516$, $Y_{\text{H}_2} = 0.00785$, $Y_{\text{He}} = 6.98 \cdot 10^{-7}$ and $Y_{\text{Ar}} = 0.0128$, as a result of the previous combustion of the first stage, where Y_k represents the mass fraction of species k. This composition yields an equivalence ratio at the inlet of the domain of $\phi = 0.35$ under the assumption of fully premixed mixture.

The mesh has a base cell size of 0.4 mm, which is about 25 times larger than the laminar flame thickness of hydrogen at 20 atm. Also, the smallest refinement corresponds to a length of approximately 50 μm, compared to the Kolmogorov length of 3-5 μm. The adaptive mesh refinement algorithm in Converge CFD is used to reduce computational cost by refining only the regions with strong gradients of velocity, up to a minimum cell size of 0.05 mm in the flame. Near the walls, an additional fixed embedding with 3 layers is used to refine the area. The typical mesh results in about 10 million cells, with a near-wall resolution within the mixing duct of $0.5 < y^+ < 3$, y^+ being the non-dimensional wall distance. The mesh quality was verified *a posteriori* using Pope's criterion for turbulent kinetic energy (TKE) [38], showing that at least 80% of the TKE is resolved in the LES. Validation of the LES results at 1 atm was performed in a previous work [17] for the same setup, showing that the LES is able to mimic well the autoignition process, of interest in the present work, at the combustor centre as compared to DNS results in [14].

3. METHODOLOGY

3.1 Non-Dimensional Analysis

Rieth *et al.* [16] showed empirically that similar flame responses can be obtained at atmospheric and high pressure conditions if the Peclet, Zeldovich, Markstein, and Lewis numbers are kept the same. The Peclet number is defined here as in [16, 39]

$$\text{Pe} = \frac{\left|\mathscr{C}_{H_2}\right|_{1D,\,max}}{\left|\mathscr{D}_{H_2}\right|_{1D,\,max}} = \frac{\left|\frac{\partial Y_{H_2}}{\partial x} u\right|_{1D,max}}{\left|\frac{1}{\rho}\frac{\partial}{\partial x}\left(\rho \frac{W_{H_2}}{W_{mix}} D_{H_2} \frac{\partial X_{H_2}}{\partial x}\right)\right|_{1D,\,max}} \quad (12)$$

where $\left|\mathscr{C}_{H_2}\right|_{1D,\,max}$ and $\left|\mathscr{D}_{H_2}\right|_{1D,\,max}$ are the maximum absolute values of convective and diffusive fluxes of H_2, W_{H_2} is the molecular weight of hydrogen and W_{mix} is the mixture molecular weight. The Zeldovich number is defined as

$$\text{Ze} = 4\frac{T_a - T_u}{T_a - T_{cross}} = \frac{E_a}{RT_a}\frac{T_a - T_u}{T_a} \quad (13)$$

where T_{cross}, T_u and T_a are respectively crossover, unburnt and adiabatic temperatures, E_a is the activation energy, and R is the universal gas constant. The effective Lewis number is [40]:

$$\text{Le}_{eff} = 1 + \frac{(\text{Le}_E - 1) + (\text{Le}_D - 1)A}{1 + A} \quad (14)$$

where Le_E and Le_D are the Lewis numbers corresponding to the excess and deficient reactants, and $A = 1 + \text{Ze}(\Phi - 1)$, with $\Phi = \phi$ in fuel rich mixtures and $\Phi = 1/\phi$ in fuel lean ones. Finally, the Markstein number is defined here as

$$\text{Ma} = \gamma_1 + \gamma_2 \text{Ze}(\text{Le}_{eff} - 1)/2 \quad (15)$$

The parameters γ_1 and γ_2 can be computed as [41]:

$$\gamma_1 = \frac{\sigma}{\sigma - 1}\int_1^\sigma \frac{\tilde{\lambda}(x)}{x}\,dx$$
$$\gamma_2 = \frac{1}{\sigma - 1}\int_1^\sigma \frac{\tilde{\lambda}(x)}{x}\ln\left(\frac{\sigma - 1}{x - 1}\right)dx \quad (16)$$

where $\tilde{\lambda}$ is the thermal conductivity and $\sigma = T_a/T_u$. The four parameters will be maintained constant in the downscaling analysis for the cases without water injection. For the case with water injection additional spray parameters are required to be downscaled, which will be discussed in Section 4.3.

3.2 Global sensitivity analysis

The goal of global sensitivity analysis (GSA) is to assess the significance of design variables in relation to factors such as thermal efficiency or NOx. This enables the exclusion of variables from future optimization processes and provides a quantitative evaluation of each variable's impact. After designing a merit function, a global sensitivity analysis can provide design directions by showing which variable is most important and how all variables interact. This type of analysis was employed in the past in compression ignition engines by several authors [42, 43], demonstrating that GSA can be an effective tool to understand the influence of parameters. To perform the spray simulations, a set of parameters is selected first to characterize the behavior
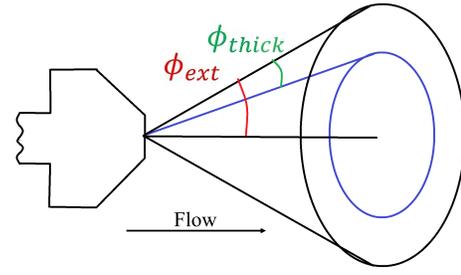
FIGURE 3: Sketch of of hollow cone geometry showing the injection angles.

of the spray. The selected parameters in this study are based on the spray characterization in a hollow cone geometry investigated in a previous study [17] and summarized in Tab. 1. These are liquid water mass flow rate $\dot{m}_w$, droplets SMD, injection angle (external angle ϕ_{ext} in the hollow cone geometry, see Fig. 3), and thickness angle ϕ_{thick}. As in [17], the injector is positioned at the center of the mixing duct, close to the inlet, and oriented in the direction of flow, like it is shown on Fig. 11. This placement was chosen to represent a generic configuration and demonstrate the performance of the proposed methodology. More complex configurations, such as altering the number of injectors, would necessitate a discrete analysis, which is incompatible with the selected global sensitivity method and therefore not suitable for this study.

Four parameters are used in this study as perfomance criteria for the GSA, namely thermal efficiency η_{th}, evaporation efficiency η_{vap}, NOx production, and pattern factor (PF), also shown in Tab. 1. While not exhaustive, this list aims to demonstrate the effectiveness of the methodology presented here, which can be adapted to specific real-life applications to identify the corresponding optimal configuration. The thermal efficiency considers losses to the isothermal walls by convection and is defined here as

$$\eta_{th} = \frac{\int_{outlets} \dot{m}h_s dA - \int_{inlets} \dot{m}h_s dA}{\dot{m}_F Q_F} \quad (17)$$

where $\dot{m}$ and h_s are mass flow rate and specific sensible enthalpy of the mixture respectively, $\dot{m}_F$ is the fuel mass flow rate and Q_F is the high heating value of the fuel. The evaporation efficiency measures the amount of droplets that are not evaporated at the exit of the combustor, and can be expressed as

$$\eta_{vap} = 1 - \frac{\int_{outlet} m_{H2O(L)}\,dA}{\dot{m}_{inj}} \quad (18)$$

where $\dot{m}_{inj}$ is the mass flow rate of the injected liquid water and $m_{H2O(L)}$ is the mass of liquid water. The pattern factor measures the homogeneity of the temperature field at the outlet, which is important because high levels of inhomogeneity (thus temperature fluctuations) at the outlet can reduce the lifetime of the turbine. This factor is defined in terms of maximum and averaged temperatures at the combustor exit section and the air temperature at the inlet as

$$\text{PF} = \frac{T_{max,out} - T_{average,\,out}}{T_{average,\,out} - T_{air}} \quad (19)$$

5

Design parameters	$\dot{m}_w$ [μg/ms]	SMD [μm]	ϕ_{ext} [deg]	ϕ_{thick} [deg]
Min. values	500	2	20	3
Max. values	15000	20	55	18
Performance parameters	η_{th}	η_{vap}	NOx	PF

TABLE 1: Summary of the design parameters, with their range of variation, and performance parameters used for the global sensitivity analysis.

Finally, NOx is evaluated as the integral value at the combustor exit in part per million (ppm) at 15% O_2. From a *black box* perspective, the GSA can be viewed as an attempt to identify the sensitivity of the function $Y = f(\boldsymbol{x})$, where $\boldsymbol{x} \in \mathbb{R}^m$ are the design parameters, presented on Tab. 1, and $Y \in \mathbb{R}^n$ are the performance parameters, also shown in the table. For the present study thus $m = n = 4$. f is the mathematical operator which here represents the numerical simulation. To obtain the sensitivity, the Sobol indices method proposed in [44] is used, consisting in decomposing the variance in the model's output into components that can be assigned to specific inputs. In the present work the first-order indices are used, which are defined as:

$$S_i = \frac{\text{Var}\left(f_i\left(x_i\right)\right)}{\text{Var}(\boldsymbol{Y})} \quad i = 1, \cdots, m \tag{20}$$

S_i measures the effect in the model's variance of the parameter x_i alone and it is normalized by the total variance $\text{Var}(\boldsymbol{Y})$ to provide a relative contribution.

A Monte Carlo method is used to calculate the sensitivity indices. This method requires an order of 1000 to 10000 model runs to calculate each index, making the computational time infeasible. Therefore, a surrogate model of our simulations is built to significantly reduce the amount of simulations required. Among various approaches for surrogate modelling [45], a Gaussian Process (GP)-based surrogate model [46] is used here as it allows to perform the GSA using a limited number of samples (20 simulations in the present study). For each performance parameter, y_α, a Gaussian Process is created. A dataset of N samples $(\boldsymbol{x}_k, y_{\alpha,k})_{k=1,\ldots,N}$ is considered, where each sample k is composed by the considered performance parameters α out of the four ($y_{\alpha,k}$), and an array composed of the four design parameters $\boldsymbol{x}_k$. A GP model can be defined for each performance parameters $\boldsymbol{x}_k$ (we drop the subscript α in the following for conciseness):

$$\hat{f}(\boldsymbol{x}) \equiv \mathbb{E}\left(Y(\boldsymbol{x}) \mid Y(\boldsymbol{x}_1) = y_1, Y(\boldsymbol{x}_2) = y_2, \ldots, Y(\boldsymbol{x}_N) = y_N\right)$$
$$= \mu_Y(\boldsymbol{x}) + \boldsymbol{\gamma}\boldsymbol{\Sigma}^{-1}(\boldsymbol{y} - \boldsymbol{\mu}) \tag{21}$$

where, naming K_Y the covariance and μ_Y the mean of the Gaus-

sian process

$$\boldsymbol{\gamma} = \left[K_Y\left(\boldsymbol{x}_1, \boldsymbol{x}\right), K_Y\left(\boldsymbol{x}_2, \boldsymbol{x}\right), \ldots, K_Y\left(\boldsymbol{x}_N, \boldsymbol{x}\right)\right]$$

$$\boldsymbol{\Sigma} = \begin{bmatrix} K_Y(\boldsymbol{x}_1, \boldsymbol{x}_1) & K_Y(\boldsymbol{x}_1, \boldsymbol{x}_2) & \ldots & K_Y(\boldsymbol{x}_1, \boldsymbol{x}_N) \\ K_Y(\boldsymbol{x}_2, \boldsymbol{x}_1) & K_Y(\boldsymbol{x}_2, \boldsymbol{x}_2) & \ldots & K_Y(\boldsymbol{x}_2, \boldsymbol{x}_N) \\ \vdots & \vdots & \ddots & \vdots \\ K_Y(\boldsymbol{x}_N, \boldsymbol{x}_1) & K_Y(\boldsymbol{x}_N, \boldsymbol{x}_2) & \ldots & K_Y(\boldsymbol{x}_N, \boldsymbol{x}_N) \end{bmatrix} \tag{22}$$

$$\boldsymbol{y} = \left[y_1, y_2, \ldots, y_N\right]^T,$$
$$\boldsymbol{\mu} = \left[\mu_Y\left(\boldsymbol{x}_1\right), \mu_Y\left(\boldsymbol{x}_2\right), \ldots, \mu_Y\left(\boldsymbol{x}_N\right)\right]^T,$$
$$\mu_Y(\boldsymbol{x}) = \sigma_0 + \sigma_1\boldsymbol{x}_1 + \cdots + \sigma_N\boldsymbol{x}_N$$

The covariance is estimated here using an exponential correlation:

$$K_Y\left(\boldsymbol{x}, \boldsymbol{x}'\right) = \tau^2 \exp\left\{-\sum_{i=1}^{m} \eta_j \left|x_i - x_i'\right| \rho_j\right\} \tag{23}$$

where $\tau = \text{Var}(Y(\boldsymbol{x}))$ is the variance of the process. The parameters $\boldsymbol{\sigma} = [\sigma_1, \ldots, \sigma_N]$, $\boldsymbol{\eta} = [\eta_1, \ldots, \eta_n]$ and $\boldsymbol{\rho} = [\rho_1, \ldots, \rho_n]$ are determined by optimizing the marginal likelihood using a conjugate gradient optimizer. A more detailed explanation of this method can be found in [47].

The GP method as defined above was cross-fold validated by using 16 samples in its construction out of the 20 LES performed in this study, and by checking its accuracy on the 4 unused samples. This process was repeated for multiple combinations and the outcomes were observed to be of similar accuracy for each combinations. Results of the GSA will be presented in Sec. 4.2.

4. RESULTS
4.1 Dry flow behaviour and flashback analysis

The terminology 'dry' case is used here to refer to the situation where no water is injected via spray. Note that a certain amount of water vapour is still present in the reactants due to the combustion in the first stage of the sequential combustor. The general flow dynamics in the combustor is represented in Fig. 4 and is as follows. Firstly, due to the high temperature set for the mixture (1180 K), autoignition occurs, leading to the development of a flame in the combustion chamber after the initial transient period. This flame exhibits a distinctive set of characteristics. The sudden expansion of the flow at the end of the mixing duct leads to the formation of large vortex structures in the corners, known as outer recirculation zone (ORZ), where hot gases are entrapped, increasing their resident time. Near the centreline the streamlines diverge due to the sudden expansion and this region is known as the Central Divergent Zone (CDZ). A shear layer is found between the ORZ and the CDZ where the flame stabilizes in propagation mode. In the CDZ autoignition is the dominant regime instead, driven by the high reactant temperature. On the other hand, the temperature of the mixture in the proximity of the walls is lower because of heat transfer to the walls, resulting in an increased ignition delay time. The ignition delay time is highly dependent on the temperature of the reactants, which is close to the crossover temperature in the studied configuration. The latter is defined for hydrogen mixtures as the temperature above which a chainbranching explosion path leads to a sudden decrease in the autoignition delay time [12, 48], which in turn
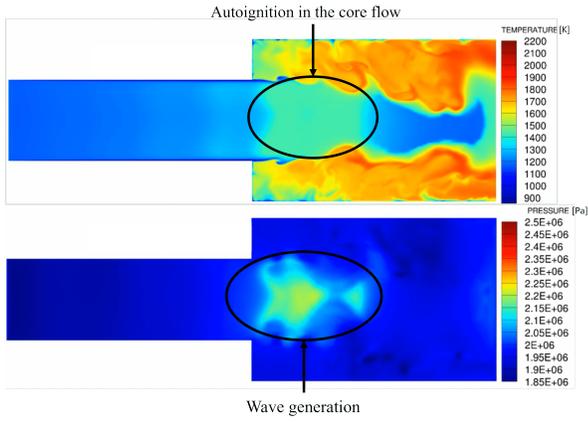
FIGURE 4: Temperature and pressure midplane contours from LES, taken 1 ms after the first detected autoignition kernel.
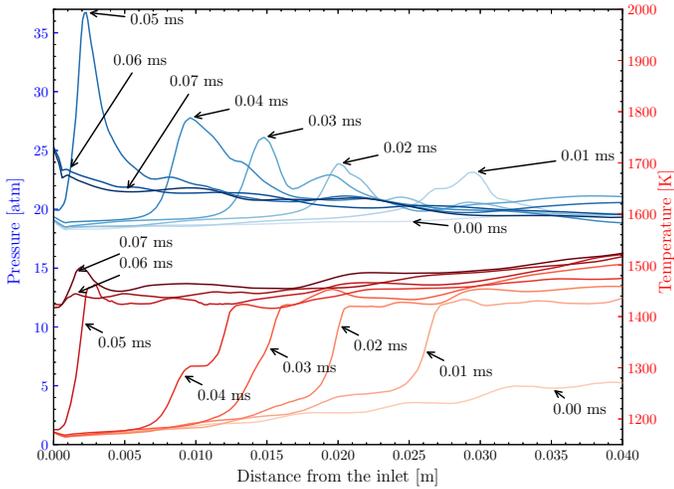
FIGURE 5: Pressure and temperature variation along the centreline of the reheat combustor as time evolves at intervals of 10 μs from the extended autoignition kernel of Fig. 4.

causes the autoignition of the reactants. For the present configuration this temperature is around 1347 K near the combustor centerline. Therefore, small variations in the reactants temperature caused by compression heating in the CDZ may trigger an early autoignition, as observed in previous studies [49].

For the highly confined geometry used for this work and the imposed boundary conditions, the following unsteady sequence of events is observed in the LES to occur at 20 atm. Starting from a situation where the flame is stabilized in propagation mode within the shear layer between ORZ and CDZ, an autoignition kernel appears in the core stream, which expands within about 1 ms in an extended autoignition region at the combustor entrance (see Fig. 4, top). This yields a rise in temperature and simultaneously an increase in pressure with expansion of the mixture. The increased pressure propagates in the form of a pressure wave (Fig. 4, bottom) in all directions. The wave propagating upstream towards the reactants is observed to be of larger amplitude than the wave moving downstream. This is shown in Fig. 5: the compression heating causes an increase of temperature above the

crossover value, so reducing the ignition delay time and pushing in turn the autoignition region further upstream. The process at this point repeats, causing a compression-driven flashback occurring at the speed of sound of the fluid, which is about 650 m/s for the present case. Once the pressure wave reaches the inlet, the piston effect stops due to the effect of the numerical boundary condition, and the pressure and temperature on the domain slowly decrease, as illustrated in Fig. 5 from 0.06 ms onwards, until the flame eventually ceases its upstream propagation and returns to its original position. It is worth noting that that the observed dynamics is an exaggeration of the behaviour in a real scenario, where fuel ramp-up is smooth and imperfect mixing leads to a variety of self ignition times, combined with a significantly more complex geometry. Nevertheless, this exaggeration is of high interest to study the flame dynamics under challenging operating conditions and assess the effectiveness of water injection (to be discussed later) in preventing flashback.

Further insight is provided in Fig. 6, showing the mass fractions of H_2O_2 and HO_2. By defining t_c as the time when the upstream-propagating flame crosses the combustor entrance section along the centreline and enters the mixing duct (flashback), these radicals are shown at two times: i) significantly ahead of the flashback, at $t = t_c - 300\ \mu$s, and ii) at $t = t_c - 60\ \mu$s. One can notice that both H_2O_2 and HO_2 concentrations start to increase significantly in the mixing duct at time $t = t_c - 60\ \mu$s (before the flashback event), indicating that both species are precursors of the flashback. An analysis on the chemical pathways shows that the reaction sequence $H_2O+H \implies HO_2 \implies H_2O_2$ is the main responsible for this increase, indicating that the key factor triggering the flashback is the presence of hydrogen radicals. According to [15], these radicals accumulate in regions of the flame with negative curvature, which leads to a strong amplification of the reaction rates at early stages of reaction progress (low temperatures), which in turn might lead to the generation of ignition kernels. Since curvature (positive and negative) is expected to be enhanced at lean conditions in hydrogen flames in particular at high pressure due to intrinsic instabilities caused by the preferential diffusion of hydrogen [16], this could partially explain the higher flashback tendency observed for the present case at 20 atm, as compared for example to the atmospheric case discussed in [17]. In the next section water injection will be used to control the flame position and prevent the occurrence of the flashback process described in this section.

4.2 Global sensitivity analysis and flashback prevention with water injection

The global sensitivity analysis with surrogate model described in Sec. 3.2 is performed on the reheat combustor at 20 atm to analyze the effect of the design variables characterizing the liquid water spray at the inlet of the mixing duct. The objective here is to stabilize the flame location and at the same time maximise/minimise the four performance parameters: thermal and evaporation efficiency, pattern factor and NOx at the combustor exit. The details for the design and performance parameters of the 20 LES performed in this study are summarised in Tab. 2. The decision to conduct a total of 20 simulations was based on the good accuracy achieved by the surrogate model trained on
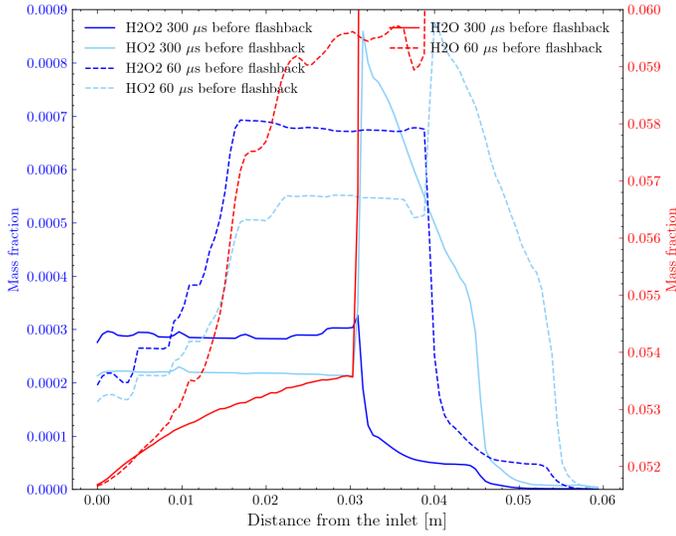
FIGURE 6: Centreline variation of H_2O_2, HO_2 and H_2O mass fractions within the reheat combustor (including mixing duct) as predicted by the LES for two times respectively 300 and 60 μs before a flashback event.

FIGURE 7: First order Sobol indices for the different performance parameters of Tab. 1, grouped according to the design parameter.

these simulations. This implies that further significant improvement of the results is not likely to be achieved. Additionally, showcasing the efficiency of the proposed procedure using a relatively low number of samples is advantageous for industry-level applications. For each individual simulation, the values of the four design parameters are randomly selected. The *bootstrap* method [50] is used for surrogate modelling. First, the collection is divided into a training and a validation group, representing 80% and 20% of the 20 samples, respectively. Then, surrogate modeling is performed and the root mean square (RMS) of the validation samples is calculated to find the most accurate model. Fig. 7 shows the first-order Sobol indices, which take into account the effect of each design parameter (inputs) on the performance parameters (outputs). There are 16 indices in total, one for each performance parameter with respect to each design parameter, denoted as $I_{o,i}$, i.e. the first order Sobol index I of performance parameter o with respect to the design parameter i. By examining the figure, the following considerations can be made:

- *Thermal efficiency* is mainly determined by the mass flow of water injected, which corresponds to an index $I_{\eta_{ther},\dot{m}_w} \approx 0.66$. The greater the amount of water injected, the greater the energy 'loss' to evaporate the droplets. The rest of the design parameters affect the thermal efficiency via the the dispersion of the droplets, but this effect is observed to be limited as shown in Fig. 7.

- *NOx production* is less straightforward. Mass flow ($I_{NOx,\dot{m}_w} \approx 0.34$), SMD ($I_{NOx,SMD} \approx 0.22$) and external angle ($I_{NOx,\phi_{ext}} \approx 0.17$) all contribute significantly to NOx production, and about in the same extent. As one can expect, a higher liquid mass flow results in lower temperatures near the flame, therefore reducing NOx via Zeldovich mechanism, which dominates at the second and third ignition limits. The effect of the external angle on NOx is also
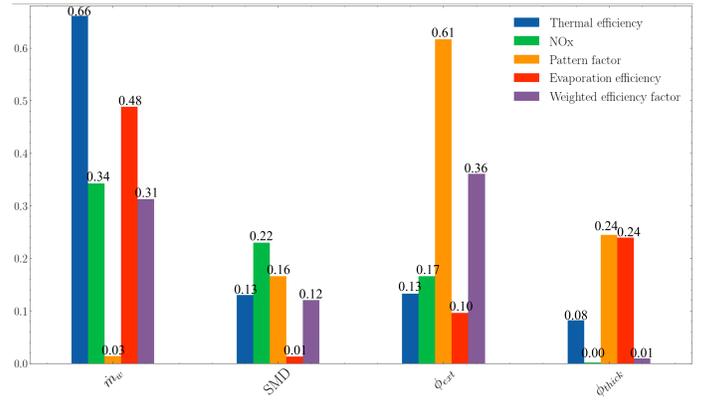
observed to be relevant. As the external angle increases, more water is able to reach the parts of the combustor that are further away from the centre, thus reducing temperature in these areas. An analysis on the chemical pathways (not shown) further indicates that NOx also reduces via the NNH and N_2O paths as result of water injection, due to the fact that the availability of O, H and OH decreases, which in turn is due to the higher concentration of HO_2 and H_2O_2 produced, that act as a sink. Finally, SMD is also observed to affect NOx. Finer droplets have less inertia and are unable to achieve optimum distribution, resulting in a concentration of droplets in the centre of the spray, which is not optimal for the suppression of temperature fluctuations. The thickness angle has instead a negligible effect on the NOx production.

- *The pattern factor* (PF) is mainly a function of the droplet distribution and this is evident in Fig. 7, since a zero index is found for the mass flow of liquid water, i.e. the amount of water injected is found to be irrelevant for the pattern factor. Of the other design parameters, the external angle ($I_{PF,\phi_{ext}} \approx 0.61$) is the most relevant for PF, indicating that a wider angle contributes to a more uniform temperature at the exit.

- *Evaporation efficiency*, η_{vap}, is mainly a function of the liquid mass flow as one would expect ($I_{\eta_{vap},\dot{m}_w} \approx 0.48$). As the mass flow increases, more droplets are unable to evaporate before reaching the outlet, resulting in an under-utilisation of water resources. The SMD is instead found to be irrelevant for η_{vap}, for the range of values considered on this analysis and displayed on Tab. 1. Although sprays with larger SMDs have a greater chance of not evaporating completely, this seems to occur only at significantly higher SMD values.

Based on the above analysis, a weighted efficiency function is defined here to approximate the overall performance of the spray in terms of the performance parameters:

$$\eta_{opt} = 0.4\eta_{therm} + 0.1\eta_{vap} + 0.45(NOx_{dry} - NOx) - 0.1PF \quad (24)$$

where the NOx is measured in ppm and $NOx_{dry} = 3.3$ ppm is the value in the dry case of Tab. 2. The weights in the above

TABLE 2: Spray design and performance parameters of the global sensitivity analysis for the 20 LES cases analysed at 20 atm.

Case	$\dot{m}_w$ [μg/ms]	SMD [μm]	ϕ_{ext} [deg]	ϕ_{thick} [deg]	η_{th}	η_{vap}	NOx [ppm]	PF
Dry	-	-	-	-	0.765	-	3.3	0.545
1	652.7	10.5	39.4	12.5	0.752	1.000	3.1	0.350
2	1084.0	15.0	27.9	13.7	0.730	1.000	3.0	0.382
3	2168.8	15.2	45.8	15.8	0.714	1.000	2.9	0.406
4	1050.8	9.1	37.8	11.9	0.752	1.000	3.0	0.382
5	2142.6	19.5	32.8	15.6	0.715	0.995	2.9	0.483
6	532.2	9.8	46.4	7.8	0.743	1.000	3.1	0.399
7	1248.1	14.1	50.6	13.7	0.731	1.000	3.3	0.532
8	2123.6	18.8	21.2	17.8	0.761	0.996	3.1	0.327
9	1047.1	6.3	32.6	17.3	0.751	0.926	3.1	0.404
10	4487.6	16.2	44.0	14.2	0.748	0.932	2.9	0.399
11	2998.6	7.0	52.9	11.4	0.739	0.999	3.1	0.380
12	3488.1	10.8	25.6	14.9	0.733	0.983	3.0	0.357
13	3851.8	12.3	42.3	9.7	0.720	1.000	2.8	0.388
14	3859.0	13.5	43.2	14.3	0.710	1.000	2.8	0.562
15	12344.3	10.7	45.4	17.3	0.737	0.743	2.9	0.455
16	5495.8	14.4	25.3	8.5	0.719	0.716	2.9	0.290
17	7937.2	17.4	27.8	11.1	0.745	0.679	2.9	0.325
18	8407.5	6.2	46.1	9.8	0.726	0.769	3.0	0.404
19	14561.6	11.6	48.9	14.1	0.711	0.740	2.8	0.475
20	4552.7	18.4	20.7	14.4	0.718	0.801	2.9	0.391

expression were assigned considering that thermal efficiency and NOx are found in the GSA to be the most relevant factors [10] as compared to the other parameters. Although the definition of η_{opt} remains somewhat arbitrary, additional analyses by varying the coefficient weights of about 10% indicates that the main conclusions to be discussed next would not change. Results obtained by applying the global sensitivity analysis to η_{opt} are shown (purple bar) in Fig. 7. One can observe that the index associated to the thickness angle is very small ($I_{\eta_{opt},\phi_{thick}} \approx 9.3 \times 10^{-3}$), implying that the effect of this parameter on the weighted efficiency factor is small. This allows to remove the thickness angle from the design process without a major loss of generality and performance. On the contrary, the external angle of the injector ϕ_{ext} has a large effect on the weighted efficiency factor ($I_{\eta_{opt},\phi_{ext}} \approx 0.36$), even larger than the injected liquid mass flow ($I_{\eta_{opt},\dot{m}_w} \approx 0.31$). This means that the choice of an appropriate external angle is a fundamental design decision. The SMD, is found to have a limited, although non-negligible, effect ($I_{\eta_{opt},SMD} \approx 0.12$).

The GSA with surrogate model is at this point used to optimize the weighted efficiency factor, in order to obtain the best set of spray parameters at a reduced computational cost. This is done by means of the well-known Broyden–Fletcher–Goldfarb–Shanno (BFGS) algorithm, which is a quasi-Newton optimization algorithm used for unconstrained nonlinear optimization problems. The outcome of this optimization is presented in Tab. 3. As compared to the baseline (unstable) dry case, this configuration presents a reduction in NOx of 17.4%, and has an evaporation efficiency $\eta_{vap} = 1$ with a relatively acceptable loss in thermal efficiency of about 3% as compared to the dry case. The weighted efficiency factor η_{opt} is 8.2 points higher than the best of the 20 calculated samples of Tab. 2. Fig. 8 demonstrates the effectiveness of this configuration in preventing

TABLE 3: Design and performance parameters of the optimized case with water injection at 20 atm found via GSA.

$\dot{m}_w$ [μg/ms]	SMD [μm]	ϕ_{ext} [deg]	ϕ_{thick} [deg]
3865.7	19.6	55.0	16.4
η_{th}	η_{vap}	NOx [ppm]	PF
0.735	1.000	2.7	0.488

flashback. The pressure wave magnitude is reduced by about 80% as compared to the dry case, from approximately 15 atm to 3 atm with the use of spray, which is significant from the point of view of the integrity of the engine components. This reduction in wave size significantly decreases the piston effect and subsequent compression heating. As shown in the graph, the flame is unable to propagate upstream through the mixing channel, implying flashback is prevented. Although some oscillations of the flame location near the wall still occurs, their amplitude is significantly reduced to approximately $2L$ in the streamwise direction, which is half that of the dry case. This analysis suggests thus the effectiveness of the GSA with surrogate model to extract design directions for combustion problems using a relatively moderate amount of computational effort.

4.3 Downscaling

The method of Rieth *et al.* [16] as described in Sec. 3.1 is used here to assess and analyse whether flashback and stable flame dynamics observed at the 20 atm condition can be maintained when downscaling the combustor to 1 atm. This information is critical as it would allow to perform experiments or more detailed simulations at low pressures to validate at least qualitatively the dynamics observed in simulations at high pressure, where the computational cost increases significantly due to
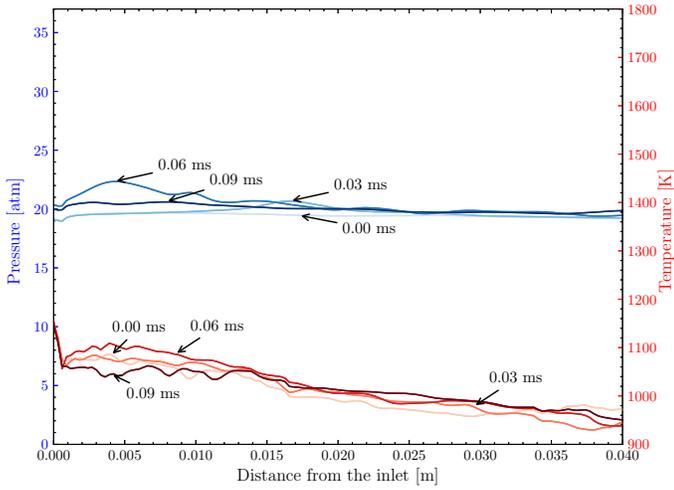
FIGURE 8: Pressure and temperature variation along the centreline of the reheat combustor as time evolves at intervals of 30 μs from the extended autoignition kernel of Fig. 4.

TABLE 4: Operative conditions and non dimensional numbers of the LES cases analysed. The first number in the case name indicates the operative pressure in atm.

Case	T_u	ϕ	Pe	Ze	Le	Ma
P20	1180 K	0.35	1.544	5.043	0.382	0.0649
P1-20	986 K	0.20	1.541	4.914	0.352	0.0732
P1	1036 K	0.35	1.130	3.700	0.402	0.576
P20-1	1200 K	0.44	1.480	4.711	0.419	0.355

FIGURE 9: Case P1-20 (top) and Case P20-1 (bottom) of Tab. 4. Case P20-1 has a smaller mixing duct so to take into account the smaller ignition delay of the mixture at 1200 K. The probe location used for Fig. 10 is also indicated in the figure.

the smaller flame thickness. In addition, from an experimental standpoint, atmospheric pressure experiments are more suitable due to the lower requirements of the selected facility and the fact that the consumables needed for such experiments are only about 5% of those required for high-pressure experiments. Four cases are studied for this analysis: (i) the dry, stable atmospheric case studied in [17], identified as case P1; (ii) the dry unstable high pressure case at 20 atm analyzed in Sec. 4.1 and identified as case P20; (iii) a downscaling from the latter to atmospheric conditions, identified as case P1-20; and (iv) an upscaling from the atmospheric to high pressure conditions at 20 atm, identified as case P20-1. These cases are summarised in Tab. 4. Both P1-20 and P20-1 cases were designed to have similar non-dimensional numbers as compared to the P20 and P1 cases, respectively. There are two factors that allow for variation in the fitting of the non-dimensional numbers: the equivalence ratio ϕ and the temperature of the reactants T_u. These two values are thus varied at the combustor inlet in order to maintain, at the different pressure, about the same values of Pe, Ze, Le and Ma. In addition, the ignition delay have to be also considered. Some combinations would imply an ignition delay very large, very small or even in some cases, the autoignition will not occur. Therefore, it is necessary to identify combinations of T_u and ϕ that also have feasible ignition delays. For those suitable combinations, the configuration exhibiting the smallest differences in nondimensional numbers is selected. Note that in Tab. 4 a larger difference exists in the Markstein number between cases P1 and P20-1, primarily attributable to the challenges in matching the four nondimensional parameters with only two degrees of freedom, T_u and ϕ, while also adhering to the constraint on the ignition delay to ensure autoignition of the flame within the domain. Nevertheless, the discrepancy in the behavior of strain with respect to flame speed, related to the variation in the Markstein number, is not substantial in this type of flame, thus a larger difference in the Markstein number can be tolerated for the present case study.

The results for cases P1-20 and P20-1 are presented in terms of midplane temperature contours in Fig. 9. The P1-20 case (downscaling from unstable 20 atm case) exhibits the presence of a flashback event, which means that, for this case, the occurrence of flashback can indeed be reproduced under atmospheric pressure conditions by choosing the equivalence ratio and the temperature of the reactants to match the Pe, Ze, Ma and Le numbers. In contrast, the flame in the P20-1 case (upscaling from stable 1 atm case) is observed to be stable (no oscillation in the axial direction). It is worth noting that a stable condition for the dry case at 20 atm could not be found in [17] by simply varying the simulation parameters, demonstrating the advantage of using this scaling approach, and opening the way to more cost-effective flashback analysis, especially when compared to computationally intensive high-pressure simulations. It is also worth noting that, although the flame is observed to be present in the mixing duct for case P20-1, this was also the case for P1 in [17]. To further elaborate on this point, time evolution of temperature in a probing location in the middle of the mixing duct is shown for the four cases of Tab. 4 in Fig. 10. It is interesting to note that for the unstable cases the frequency of the flashback events (indicated by the observed peaks of temperature) is similar after the downscaling. For the stable case, after the upscaling at 20 atm some stronger oscillations is observed in time signal, indicating the presence of compression heating at the probing point location. Nevertheless, this does not lead to ignition and flashback.

Water injection was used in Sec. 4.2 to suppress the flashback observed for the dry case at 20 atm. It is at this point interesting to assess whether the scaling method of Rieth *et al.* [16] can be extended to up/downscaling also cases involving water injection. Since the spray characteristics change with the operative pressure,
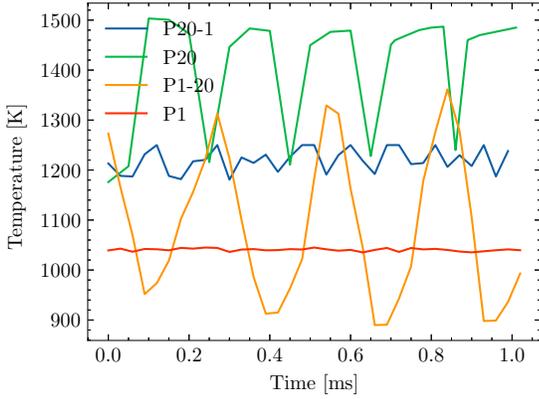
FIGURE 10: Temperature behaviour in time at the probe location indicated in Fig. 9 for the four cases of Tab. 4.

TABLE 5: Design and performance parameters for case P1-20 of Tab. 4, showing dry and three different water injection conditions.

Case	$\dot{m}_w$	SMD [μm]	p_{in} [MPa]	η_{th}	η_{vap}	NOx
Dry	-	-	-	0.735	-	0.5
SC1	68.0	19.6	7.2	0.72	0.552	0.3
SC2	68.0	11.2	7.2	0.699	0.901	0.2
SC3	120	5.0	45.9	0.698	1	0.2

FIGURE 11: Case P1-20 of Tab. 4 with water injection conditions SC1 (left), SC2 (centre) and SC3 (right) of Tab. 4. Position of the injector, which injects the droplets towards the combustor chamber forming a cone (left)

.

it is in fact expected that the multi-phase dynamics of the water droplets within the combustor after downscaling will be different. Indeed, applying the scaling as it is to the stable condition at 20 atm with water injection (i.e. without modifying the water parameters) results in a too-strong flux of water at 1 atm, implying very poor thermal and evaporation efficiencies (not shown). Three different scaling options shown in Table 5 are thus tested here for the water injection, and results in terms of midplane temperature contours are shown in Fig. 11. The first attempt, SC1, consists in scaling the water mass flow proportionally to the amount of injected fuel, and maintaining the water-to-fuel ratio of the optimized case at 20 atm unaltered, $\dot{m}_w/\dot{m}_f = 3.2$. The second attempt, SC2, consists in linearly scaling both water mass flow and SMD proportionally to the amount of fuel injected. In the third attempt, SC3, droplet velocity and SMD are varied. Flashback is shown to be prevented at 1 atm only when using the scaling options SC2 and SC3, although a flame near the walls in the mixing duct is still observed for these cases, indicating that the spray angle also needs to be changed, which is however beyond the scope of the present study. The flashback for case SC1 is caused by a poor evaporation efficiency ($\eta_{vap} = 0.552$) combined with a poor dispersion of particles. For case SC2, the water droplets evaporate more easily due to the lower SMD of 11.2 μm. However, there is a high concentration of droplets near the centerline because the particles lack sufficient inertia to achieve a high degree of dispersion, resulting in η_{vap} still below unity. The results for cases SC1 and SC2 suggest that a simple scaling of mass flow is not enough to mimic the performance of the high pressure case. For this reason the SMD is further decreased in case SC3 to guarantee that all the particles evaporate before leaving the domain. The injection pressure is increased (implying higher massflow rate of liquid water) to have more energetic droplets and thus reach a higher degree of dispersion. This case results in evaporation efficiency of 1 with a thermal efficiency loss of only 3.7%. NOx is also observed to significantly reduce (about 33%). This reduction is significantly stronger than that observed at 20 atm when water injection is used, with a similar 'loss' in thermal efficiency, which is partly due to the fact that the heat capacity of the dry mixture is lower for the case at 1 atm due to the lower reactants temperature.

5. CONCLUSION

Large eddy simulations have been performed using a thickened flame approach and detailed chemistry in a simplified geometry of the hydrogen-fuelled reheat combustor within the Ansaldo GT36 gas turbine, where the hydrogen flame is stabilized by means of assisted autoignition. Due to the confined geometry and simplifications made with respect to the real engine, strong flame instabilities are present at high pressures as a result of the early occurrence of the autoignition kernel, generating pressure waves which travel upstream and cause compression heating, which in turn decrease the ignition delay time near the centreline and triggers a sudden flashback. Liquid water injection has been used in the attempt to control the occurrence of these ignition kernel and thus prevent the flashback. Global sensitivity analysis with a surrogate Gaussian-based model has been performed to find the optimal spray condition using a total of 20 simulations where the injection angle, SMD, thickness, and external angle of the spray cone are varied to stabilize the flame at the combustor entrance while maximizing thermal and evaporation efficiency as well as minimizing NOx and pattern factor. Results indicate that the external angle of the cone is the most important parameter for achieving an optimal solution, while the thickness angle can be disregarded. An optimized solution that can prevent the flashback event has been found, which is able to reduce the pro-

duction of NOx of about 17%, keeping an evaporation efficiency $\eta_{vap} = 1$ and a loss of thermal efficiency of about 3%. This significant reduction of oscillations and flashback through water injection observed in the LES suggests a positive outlook for its implementation in actual engines.

A downscaling method has also been performed in order to assess whether the same flame dynamics observed at high pressure can be observed at low pressure and *vice versa*, in particular whether stable or unstable conditions can be reproduced. The method proves successful in reproducing the general flame dynamics in the cases where no water injection is used. Attempts have been made to extend the scaling method to the spray parameters in the case of the LES with water injection. Results show that, although a strong scaling is not obtained, with a small adjustment in some of the spray parameters it is possible to obtain a satisfactory solution. These results are promising in light of the possibility of analyzing the combustor and spray performance at different pressure conditions and thus aid the design process of new-generation combustion devices.

ACKNOWLEDGMENTS

REFERENCES

[1] International Energy Authority. *World Energy Outlook 2022*. Paris (2022). URL https://www.iea.org/reports/world-energy-outlook-2022.

[2] Lammel, G. and Graßl, H. "Greenhouse effect of NOx." *Environ. Sci. Pollut. R.* Vol. 2 No. 1 (1995): p. 40–45.

[3] Benim, A. C. and Syed, K. J. *Flashback Mechanisms in Lean Premixed Gas Turbine Combustion*. Elsevier Academic Press (2014).

[4] Strohle, J. and Myhrvold, T. "An Evaluation of Detailed Reaction Mechanisms for Hydrogen Combustion Under Gas Turbine Conditions." *Int. J. Hydrogen Energy* Vol. 32 No. 1 (2007): pp. 125–135.

[5] Bhargava, A., Colket, M., Sowa, W., Casleton, K. and Maloney, D. "An Experimental and Modeling Study of Humid Air Premixed Flames." *J. Eng. Gas Turbines Power* Vol. 122 No. 3 (2000): pp. 405–411.

[6] Nemitallah, M., Rashwan, S., Mansir, I., Abdelhafez, A. and Habib, M. A. "Review of Novel Combustion Techniques for Clean Power Production in Gas Turbines." *Energy Fuels* Vol. 32 No. 2 (2018): pp. 979–1004.

[7] Lellek, S., Barfuß, C. and Sattelmayer, T. "Experimental Study of the Interaction of Water Sprays With Swirling Premixed Natural Gas Flames." *J. Eng. Gas Turbines Power* Vol. 139 No. 2 (2016): p. 021506.

[8] Tanneberger, T., Schimek, S., Paschereit, C. O. and Stathopoulos, P. "Combustion Efficiency Measurements and Burner Characterization in a Hydrogen-Oxyfuel Combustor." *Int. J. Hydrogen Energy* Vol. 44 No. 56 (2019): pp. 29752–29764.

[9] Amani, E., Akbari, M.R. and Shahpouri, S. "Multi-Objective CFD Optimizations of Water Spray Injection in Gas-Turbine Combustors." *Fuel* Vol. 227 (2018): pp. 267–278.

[10] Farokhipour, A., Hamidpour, E. and Amani, E. "A Numerical Study of NOx Reduction by Water Spray Injection in Gas Turbine Combustion Chambers." *Fuel* Vol. 212 (2018): pp. 173–186.

[11] Pappa, A., Bricteux, L., Bénard, P. and De Paepe, W. "Can Water Dilution Avoid Flashback on a Hydrogen-Enriched Micro-Gas Turbine Combustion?—A Large Eddy Simulations Study." *J. Eng. Gas Turbines Power* Vol. 143 No. 4 (2021): p. 041008.

[12] Gruber, A., Heggset, T., Duesing, M. and Ciani, A. "A Numerical Investigation of Reheat Hydrogen Combustion in a Simplified Geometrical Configuration From Atmospheric Pressure to Full Load Conditions." *ASME Turbo Expo*, Vol. 3B. GT2022-83218. 2022.

[13] Noble, D., Wu, D., Emerson, B., Sheppard, S., Lieuwen, T. and Angello, L. "Assessment of Current Capabilities and Near-Term Availability of Hydrogen-Fired Gas Turbines Considering a Low-Carbon Future." *J. Eng. Gas Turbines Power* Vol. 143 No. 4 (2021): p. 041002.

[14] Aditya, K., Gruber, A., Xu, C., Lu, T., Krisman, A., Bothien, M. R. and Chen, J. H. "Direct Numerical Simulation of Flame Stabilization Assisted by Autoignition in a Reheat Gas Turbine Combustor." *Proc. Combust. Inst.* Vol. 37 No. 2 (2019): pp. 2635–2642.

[15] Rieth, M., Gruber, A., Williams, F. A. and Chen, J. H. "Enhanced Burning Rates in Hydrogen-Enriched Turbulent Premixed Flames by Diffusion of Molecular and Atomic Hydrogen." *Combust. Flame* Vol. 239 (2022): p. 111740.

[16] Rieth, M., Gruber, A. and Chen, J. H. "The Effect of Pressure on Lean Premixed Hydrogen-Air Flames." *Combust. Flame* Vol. 250 (2023): p. 112514.

[17] Kruljevic, B., Cabello, A., Ciani, A., Langella, I. and Duesing, M. "LES/Thickened Flame Model of Reheat Hydrogen Combustion With Water/Steam Injection." *ASME Turbo Expo*. GT2023-103466. 2023.

[18] Gruber, A., Bothien, M. R., Ciani, A., Aditya, K., Chen, J. H. and Williams, F. A. "Direct Numerical Simulation of Autoignition-Enhanced Flame Stabilization in a Hydrogen-Fueled Reheat Gas Turbine Combustor." *J. Eng. Gas Turbines Power* Vol. 69 No. 5 (2021).

[19] *GT36 First Stage Development Enabling Load and Fuel (H2) Flexibility With Low Emissions*. ASME Turbo Expo (2023).

[20] Wang, G., Boileau, M. and Veynante, D. "Implementation of a Dynamic Thickened Flame Model for Large Eddy Simulations of Turbulent Premixed Combustion." *Combust. Flame* Vol. 158 No. 11 (2011): pp. 2199–2213.

[21] Schulz, O., Jaravel, T., Poinsot, T., Cuenot, B. and Noiray, N. "A Criterion to Distinguish Autoignition and Propagation Applied to a Lifted Methane–Air Jet Flame." *Proc. Combust. Inst.* Vol. 36 No. 2 (2017): pp. 1637–1644.

[22] Charlette, F., Meneveau, C. and Veynante, D. "A Power-Law Flame Wrinkling Model for LES of Premixed Turbulent Combustion Part II: Dynamic Formulation." *Combust. Flame* Vol. 131 No. 1–2 (2002): pp. 181–197.

[23] Li, J., Zhao, Z., Kazakov, A. and Dryer, F. L. "An Updated Comprehensive Kinetic Model of Hydrogen Combustion." *Int. J. Chem. Kinet.* Vol. 36 No. 10 (2004): pp. 566–575.

[24] Olm, C., Zsély, I. G., Pálvölgyi, R., Varga, T., Nagy, T., Curran, H. J. and Turányi, T. "Comparison of the Performance of Several Recent Hydrogen Combustion Mechanisms." *Combust. Flame* Vol. 161 No. 9 (2014): pp. 2219–2234.

[25] Amsden, A. A., O'Rourke, P. J. and Butler, T. D. *KIVA-II: A computer program for chemically reactive flows with sprays* (1989).

[26] Crowe, C. T., Schwarzkopf, J. D., Sommerfeld, M. and Tsuji, Y. *Multiphase Flows with Droplets and Particles*. Taylor & Francis CRC Press (2011).

[27] Jones, W. P., Marquis, A. J. and Dongwon, N. "An Investigation of a Turbulent Spray Flame Using Large Eddy Simulation With a Stochastic Breakup Model." *Combust. Flame* Vol. 186 (2017): pp. 277–298.

[28] Rittler, A., Proch, F. and Kempf, A. M. "LES of the Sydney Piloted Spray Flame Series With the PFGM/ATF Approach and Different Sub-Filter Models." *Combust. Flame* Vol. 162 (2015): pp. 1575–1598.

[29] Schmidt, D. P. and Rutland, C. J. "A New Droplet Collision Algorithm." *J. Comput. Phys.* Vol. 164 No. 1 (2000): pp. 62–80.

[30] Rodhiya, A., Aditya, K., Gruber, A. and Chen, J. H. "Simulations of flame structure in a reheat burner: pressure scaling." *AIAA Propulsion and Energy 2021 Forum*. 2021. AIAA.

[31] Bothien, M. R., Ciani, A., Wood, J. P. and Fruechtel, G. "Toward Decarbonized Power Generation With Gas Turbines by Using Sequential Combustion for Burning Hydrogen." *J. Eng. Gas Turbines Power* Vol. 141 No. 12 (2019): p. 121013.

[32] *Large-Eddy Simulation of Turbulent Flow Over and Around a Cube in a Plate Channel*. Proceedings of the Eighth Symposium on Turbulent Shear Flows (1993).

[33] Han, Zhiyu and Reitz, Rolf D. "A temperature wall function formulation for variable-density turbulent flows with application to engine convective heat transfer modeling." *Int. J. Heat Mass Transfer* (1997).

[34] Yoshizawa, A. and Horiuti, K. "A Statistically-Derived Subgrid-Scale Kinetic Energy Model for the Large-Eddy Simulation of Turbulent Flows." *J. Phys. Soc. Jpn.* Vol. 54 No. 8 (1985): pp. 2834–2839.

[35] Menon, S., Yeung, P. K. and Kim, W. W. "Effect of Subgrid Models on the Computed Interscale Energy Transfer in Isotropic Turbulence." *Computers & Fluids* Vol. 25 No. 2 (1996): pp. 165–180.

[36] Redlich, O. and Kwong, J. N. S. "On the Thermodynamics of Solutions. V. An Equation of State. Fugacities of Gaseous Solutions." *Chem. Rev.* Vol. 44 No. 1 (1949): pp. 233–244.

[37] Thompson, K. W. "Time Dependent Boundary Conditions for Hyperbolic Systems." *J. Comput. Phys.* Vol. 68 No. 1 (1987): pp. 1–24.

[38] Pope, S. B. "Ten Questions Concerning the Large-Eddy Simulation of Turbulent Flows." *New. J. Phys.* Vol. 6 No. 1 (2004): p. 35.

[39] Jomaas, G., Law, C. K. and Bechtold, J. K. "On Transition to Cellularity in Expanding Spherical Flames." *J. Fluid Mech.* Vol. 583 No. 1 (2007): pp. 1–26.

[40] Bechtold, J.K. and Matalon, M. "The dependence of the Markstein length on stoichiometry." *Combust. Flame* Vol. 127 No. 1–2 (2001): p. 1906–1913.

[41] Addabbo, R., Bechtold, J. K. and Matalon, M. "Wrinkling of Spherically Expanding Flames." *Proc. Combust. Inst.* Vol. 29 No. 2 (2002): pp. 1527–1535.

[42] Kodavasal, J., Pei, Y., Harms, K., Ciatti, S., Wagner, A., Senecal, P., García, M. and Som, S. "Global Sensitivity Analysis of a Gasoline Compression Ignition Engine Simulation with Multiple Targets on an IBM Blue Gene/Q Supercomputer." 2016.

[43] Pal, P., Probst, D., Pei, Y., Zhang, Y., Traver, M., Cleary, D. and Som, S. "Numerical Investigation of a Gasoline-Like Fuel in a Heavy-Duty Compression Ignition Engine Using Global Sensitivity Analysis." *SAE Int. J. Fuels. Lubr.* (2017).

[44] Sobol, I. M. "Global Sensitivity Indices for Nonlinear Mathematical Models and Their Monte Carlo Estimates." *Math. Comput. Simul.* Vol. 55 No. 1–3 (2001): pp. 271–280.

[45] Storlie, C. B., Swiler, L. P., Helton, J. C. and Sallaberry, C. J. "Implementation and Evaluation of Nonparametric Regression Procedures for Sensitivity Analysis of Computationally Demanding Models." *Reliab. Eng. Syst. Saf.* Vol. 94 No. 11 (2009): pp. 1735–1763.

[46] Sacks, J., Welch, W. J., Mitchell, T. J. and Wynn, H. P. "Design and Analysis of Computer Experiments." *Statist. Sci.* Vol. 4 No. 4 (1989): pp. 409–423.

[47] Rasmussen, C. E. and Williams, C. K. I. *Gaussian Processes for Machine Learning*. MIT Press (2005).

[48] Álamo, G., Williams, F. A. and Sánchez, A. L. "Hydrogen–Oxygen Induction Times Above Crossover Temperatures." *Combust. Sci. Technol.* Vol. 176 No. 10 (2004): pp. 1599–1626.

[49] Hawkes, E. R., Sankaran, R., Pébay, P. P. and Chen, J. H. "Direct Numerical Simulation of Ignition Front Propagation in a Constant Volume With Temperature Inhomogeneities." *Combust. Flame* Vol. 145 No. 1–2 (2006): pp. 145–159.

[50] James, G., Witten, D., Hastie, T. and Tibshirani, R. *An Introduction to Statistical Learning: with Applications in R*. Springer Nature (2021).